2014

Grain size and particle dispersion effects on the tensile behavior of friction stir welded MA956 oxide dispersion strengthened steel from low to elevated temperatu

Materials Science & Engineering A 589 (2014) 217–227

Contents lists available at ScienceDirect

Materials Science & Engineering A

journal homepage: www.elsevier.com/locate/msea

Grain size and particle dispersion effects on the tensile behavior of friction stir welded MA956 oxide dispersion strengthened steel from low to elevated temperatures

B.W. Baker*, T.R. McNelley, L.N. Brewer

Naval Postgraduate School, 700 Dyer RD, Watkins Hall Room 331, Monterey, CA 93943-5100, USA

ARTICLE INFO

Article history:
Received 26 June 2013
Received in revised form
17 September 2013
Accepted 26 September 2013
Available online 4 October 2013

Keywords:
Friction stir welding
Oxide dispersion strengthened steel
MA956

ABSTRACT

This paper shows the dependence of tensile behavior of friction stir welded oxide dispersion strengthened steel (MA956) on testing temperature and welding parameters. Eight welding conditions were utilized and three produced consolidated defect-free welds in MA956 plate material. Tensile samples were prepared from the welded plate and were subjected to tensile testing with a strain rate of 10^{-3} s^{-1} over temperatures from ambient to 600 °C. The base plate material possessed a fine-grained microstructure that exhibited limited ductility, high yield strength, and moderate strain hardening at low temperatures. At elevated temperatures the base plate was more ductile and possessed limited strain hardening. Friction stir welding caused a significant (42%) reduction in yield strength at low temperatures and a corresponding increase in ductility compared to the base plate material. These changes became more pronounced as the heat input increased. The change in tensile behavior was the result of ferrite grain and oxide particle coarsening. The effect of grain coarsening was well-described by the Hall–Petch relationship and oxide particle coarsening resulted in the loss of particle strengthening.
Published by Elsevier B.V.

1. Introduction

Although initially designed for use in high temperature gas turbine applications, the high temperature strength, radiation damage resistance, creep resistance, and corrosion resistance of oxide dispersion strengthened (ODS) steels, such as MA956, make these alloys potential candidates for use in next generation nuclear power production applications [1–5]. The extremely fine, homogenously dispersed oxides in ODS steels give these materials exceptional high-temperature strength due to the pinning of grain boundaries and dislocations. These dispersed oxides also provide sites for the accumulation of hydrogen and helium atoms that can mitigate the effects of radiation-induced swelling in nuclear applications.

As appealing as MA956 and other ODS steels are for nuclear applications, joining structural components comprised of ODS alloys is a key technology challenge limiting their use [6–10]. To address this issue, numerous research studies have shown that conventional fusion welding and other high temperature joining techniques of ODS alloys are problematic due to agglomeration of oxide particles which causes inconsistent material performance in particle depleted areas [11–14]. The solid state joining technique friction stir welding (FSW), has been shown to be effective for MA956 and other ODS alloys by several authors [15–20], but a systematic review of FSW conditions, evolved microstructure, and final material properties has not been completed. Baker et al. have recently shown that FSW can produce consolidated welds in ODS steels with varying degrees of grain coarsening depending on the starting grain size [21]. Additional work has conclusively shown that FSW causes significant oxide particle coarsening which reduces the strengthening contribution of the dispersed oxides considerably [22]. The research presented herein combined with related reports on the evolved microstructure [21] and oxide particle morphology [22] aims to establish the processing, microstructure, and material property relationships of the ODS alloy MA956 following FSW with a variety of welding conditions. When combined the results show that MA956 can be manufactured and joined in a manner that maintains sufficient high temperature strength for use in nuclear applications.

The initial grain size of MA956 plays a prominent role in the yield strength of the base alloy via the Hall–Petch relationship and in the evolved material properties following FSW due to grain refinement (typical after FSW of coarse grained materials) or grain coarsening (typical after FSW of fine grained materials). For the purposes of this research, MA956 with an average grain size of less than 100 μm is denoted as fine grain (FG), unrecrystallized material; whereas MA956 with an average grain size of greater than 100 μm

* Corresponding author. Tel.: +1 831 656 2213; fax: +1 831 656 2238.
E-mail addresses: bwbaker@nps.edu, bradfordbaker@hotmail.com (B.W. Baker), trmcnelley@nps.edu (T.R. McNelley), lnbrewer@nps.edu (L.N. Brewer).

0921-5093/$ - see front matter Published by Elsevier B.V.
http://dx.doi.org/10.1016/j.msea.2013.09.092

is denoted as coarse grain (CG), recrystallized material. Although no absolute standard exists, this denotation is consistent with other literature, and both FG and CG versions of MA956 are available depending on the intended application, although most research is based on CG materials (normally grain sizes of 100s of μm or more) including Special Metals published data [23–29]. Limited research has been completed on the microstructure–mechanical property relationships for FG MA956 although some theoretical and experimental data exists on FG MA956 which emphasizes the significance of the fine grain size on base material performance such as yield strength [30,31], ductility [32], and creep resistance [33,34]. The line between FG and CG material is intended to be broad division that is based on the desired application and is achieved by an intentional post-manufacture heat treatment. The MA956 used in this research is considered a FG material even after FSW even though it will be shown that FSW causes dramatic grain coarsening.

Because of creep concerns in FG alloys, MA956 was originally designed to be manufactured in CG form for gas turbine applications including potential single crystal turbine blade designs [24]; however, other research on MA956 has shown that the creep behavior of FG MA956 may be sufficiently close to CG MA956 to allow for its use in high temperature applications while capitalizing on the improved strength and radiation damage resistance of the FG design [33,34]. Specifically, research showed that MA956 with fine elongated grains had minimum creep rates that were comparable to MA956 with coarse elongated grains. This creep evaluation of FG alloys is consistent with research on other ODS alloys such as 12YWT that show promising creep performance when compared to traditional ferritic-martensitic steels [35,36].

Previous research on FSW of MA956 has shown that FSW is a viable joining mechanism that can produce consolidated welds in MA956 while maintaining a majority of the base material hardness [21,29,37]. Research on FSW with an initial fine grain size was shown to cause significant grain coarsening and softening in the weld nugget that was a function of the welding parameters [21]. Weld consolidation, grain growth, texture, and hardness were correlated to welding parameters using a ratio of tool rotational speed (ω) in revolutions per minute (RPM) to tool traverse speed (ν) in millimeters per minute (MMPM) denoted as heat index (HI) (Eq. (1)). This method is consistent with other research that uses HI as a measure of the welding heat input and evaluate weld consolidation, evolved microstructure, and material properties following FSW for a variety of materials in relation to this parameter [38–41].

$$HI = \frac{\omega}{\nu}. \tag{1}$$

The objective of this paper is to characterize the tensile deformation properties of FG MA956 as a function of testing temperature for both the base metal (BM) and the stir zone (SZ) material following FSW. The terminology of BM and SZ is consistent with discussions of FSW by Mishra [38] with the SZ representing the center of the weld nugget and the BM representing areas outside of the heat affected zones and thermo-mechanically affected zones on both sides of the weld pass. As the welded microstructure evolves significantly from the base plate material, special attention is given to the role of welding conditions on the resultant tensile properties and their temperature dependence. Finally, the overall processing, microstructure, and tensile deformation relationships following FSW are presented. The results show that FG MA956 is a useful high strength alloy for elevated temperature applications and that FSW is a viable joining technique for MA956 that maintains most of the alloy's high temperature strength, while sacrificing a significant amount of the lower temperature strength of the joint.

2. Experimental procedure

The MA956 used was a high Cr ferritic ODS steel with the material composition shown in Table 1. Composition data was acquired using inductively coupled plasma mass spectrometry and LECO analysis (Anamet Inc., Hayward, CA). MA956 powder was canned and extruded by Special Metals at 1100 °C (2025 °F) and subsequently hot-rolled in three passes at 1100 °C (2025 °F) over 4 h with reheating to 1100 °C (2025 °F) for 30 min before and after each rolling pass. Unlike most production processes of MA956 done by Special Metals, the MA956 in this research was not exposed to any additional heat treatment after hot rolling. Final machining provided a 4 mm (0.157 in.) thick plate. As shown in previous results, this manufacturing process produces a FG unrecrystallized MA956 base material. Manufacturing techniques for most other MA956 research and applications include a post-manufacture heat treatment that produces a CG recrystallized MA956 base material.

FSW of MA956 plate was accomplished by MegaStir Technologies, Provo, UT using a tool fabricated from an MS 80 grade of polycrystalline cubic boron nitride (PCBN) and having a convex scroll shoulder step spiral (CS4) tool design which requires no tool tilt. FSW parameters of tool rotation rate in RPM (300–500 RPM) and tool traverse speed in (25–100 MMPM) were varied to produce eight differing weld conditions. Plunge force was maintained constant at 17.8 kN (4000 lbf). For the current paper, only fully consolidated welds were analyzed although previous research on processing and microstructure relationships included defective welds [21]. The three defect free FSW parameter conditions analyzed in this paper are (1) 400 RPM/100 MMPM (the lowest heat input condition), (2) 300 RPM/50 MMPM (slightly higher heat condition), and (3) 500 RPM/25 MMPM (the highest heat input condition).

Tensile specimens (gage section dimensions: length = 12.7 mm, width = 5.08 mm, and thickness = 1.09 mm) were manufactured from SZ and BM sections of MA956 via electrical discharge machining. Friction stir welded specimens were oriented such that the specimen gage length was perpendicular to both the welding and rolling direction and the entire gage length consisted of SZ material (Fig. 1). BM specimens were similarly oriented from plate material that had not been friction stir welded. Two maximize material usage,

Table 1
Chemical composition of MA956 (wt%).

C	Cr	Al	Ti	Y_2O_3	Mo	Mn	Ni	S	Si	P	Fe
0.023	19.93	4.75	0.39	0.51	0.02	0.09	0.04	0.008	0.08	0.006	Bal.

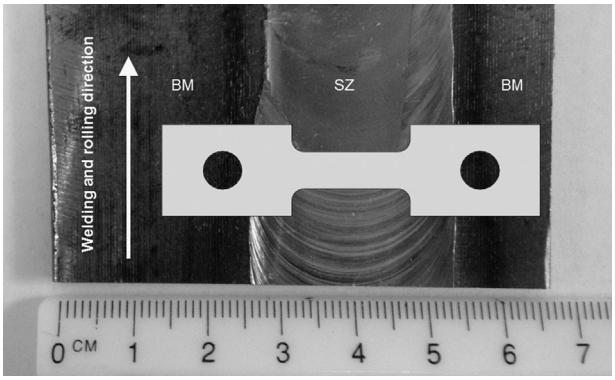

Fig. 1. Tensile specimen geometry (gage section measurements: length = 12.7 mm, width = 5.08 mm, and thickness = 1.09 mm) with corresponding location with respect to welded plate. Stir zone (SZ) annotated as the center of the weld pass and base metal (BM) annotated on each side of the weld pass.

two tensile specimens were machined from each specimen location indicated in Fig. 1 (i.e. one specimen on top of the other through the thickness of the plate). This decision was based on previous hardness research on the same plate that showed that there was minimal vertical hardness variation in the center of the SZ corresponding to the gage section of the tensile specimen [21].

The primary consideration for tensile specimen design was conservation of material since a limited amount of MA956 was available. A secondary consideration was to ensure that the gage section consisted entirely of SZ material. Previous research showed that large gradients in microstructure and hardness exist at the retreating side (RS) and advancing side (AS) of the weld nugget, and the gage section of the tensile specimen was intentionally designed to avoid any possible effects from these gradients. Extensive literature review and finite element modeling was conducted to verify the suitability of the specimen geometry prior to testing, and although the specimen geometry does not conform to an ASTM standard, it is similar to those used or proposed for use in miniature mechanical testing of irradiated materials [42–46]. The specific aspects considered were the aspect ratio of the specimen (defined as the thickness to width ratio of the gage section) and the radius of curvature from the grip to the gauge section to ensure that yield stress and ultimate strain values were not adversely affected by design and that failure would occur in the gage section.

Tensile tests were conducted using an INSTRON 4507 load frame with a 10 kN load cell. Constant extension rate tests were conducted at a crosshead speed of 0.762 mm/min equating to a maximum tensile strain rate of $10^{-3}\,s^{-1}$ for the specimen geometry. Although considered, insufficient material existed to conduct strain rate sensitivity tests; therefore, all tensile tests were conducted at the same crosshead speed. Additionally research by Salomon on MA956 concluded that strain rate sensitivity began at temperatures around 600 °C which was the upper end of the temperature range for this research [32]. Tests were conducted at room temperature (20 °C) and at temperatures up to 600 °C (± 5 °C) using a 4800 W Applied Test Systems five-zone tubular furnace that enclosed the entire specimen and grip connections of the load frame. For tests at temperatures above room temperature, specimens were manually maintained at a small tensile load (<50 N equating to less than 5% of the yield stress) for 1 h to allow for thermal equilibration prior to testing. BM specimens were tested at room temperature, 400 °C, 500 °C, and 600 °C. Due to limited availability of friction stir welded specimens and the relative consistency of the BM response between 400 °C and 600 °C, the three FSW conditions were tested at room temperature, 400 °C and 600 °C.

Because of the small specimen size and the elevated temperature testing, an extensometer was not used and strain was calculated using crosshead displacement. The potential errors in strain measurement using crosshead displacement alone are discussed elsewhere in the literature [47,48]. To compensate, instrumented testing at room temperature using strain gages was conducted on the same geometry using other materials and the effect of machine compliance in the elastic region was removed as discussed in [48]. This machine compliance adjustment has negligible effect on yield or ultimate tensile strength measurements, but gives improved accuracy in total elongation measurements versus using crosshead displacement alone.

To verify the tensile procedures described above, tensile testing was conducted on a series of SS316 samples of identical geometry prior to testing on MA956. A work-hardened SS316 was selected as a candidate test material based on its similarity to MA956, availability, and abundance of data in the open literature. Full details of the SS316 results are presented elsewhere [22], but appropriate tensile property values and trends in performance were observed for SS316 at temperatures up to 600 °C including yield strength, ultimate tensile strength, percent elongation, work hardening, ductility minima, and serrated flow regimes. Since insufficient MA956 material was available for multiple specimen testing at each condition, the variations in experimental data for SS316 at room temperature were applied as experimental error for MA956. The variations in yield strength, ultimate tensile strength, and percent elongation for SS316 at room temperature were all less than 5% (Table 2).

Fractography of specimens was conducted using a Zeiss Neon 40 field emission scanning electron microscope (SEM) operating at 20 keV. High magnification imaging was conducted with no specimen tilt and at a low working distance (5 mm) to allow for improved focus. High magnification imaging was taken in representative areas of the fracture surface near the center of the specimen. Low magnification imaging was conducted with specimens tilted at 10° and at a larger working distance (approximately 15 mm) to allow for full visualization of the fractured sample.

3. Results

3.1. Base metal properties

Similar to the CG results published by Special Metals [23], FG MA956 at room temperature had limited ductility (ε_f=0.118 mm/mm), but a significantly higher strength (σ_y=909 MPa and σ_{uts}=991 MPa) due to grain refinement (Fig. 2). At 400 °C FG MA956 exhibited little change in ductility but a significant reduction in strength. Increasing the test temperature to 600 °C caused an increase in ductility (ε_f=0.485 mm/mm) and further reduction in strength (σ_y=292 MPa and σ_{uts}=309 MPa) (Fig. 2). Unlike SS316, no serrated flow regimes were observed in FG MA956 at any temperature up to 600 °C.

Table 2
Variability of SS316 tensile testing at room temperature showing less than 5% variation in tensile parameters for the given experimental setup.

Sample	Yield strength (MPa)	Ultimate tensile strength (MPa)	Percent elongation (%)
SS316-1	502	735	56.8
SS316-2	499	737	56.1
SS316-3	522	742	54.4
SS316-4	501	732	54.9
SS316-5	501	737	54.5

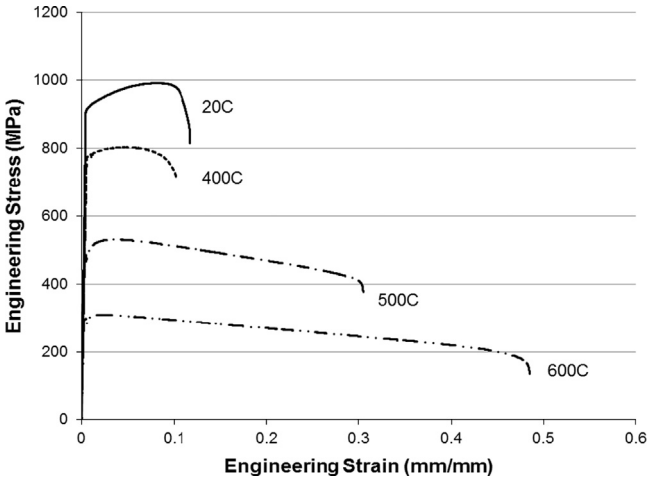

Fig. 2. Engineering stress–strain curves for base metal MA956 at various temperatures.

Fractography of BM specimens was consistent with observations during tensile testing at all temperatures. At room temperature, MA956 exhibited very limited reduction in area and the fracture surface was characterized by large faceted transgranular fracture surfaces indicative of brittle failure (Fig. 3a and b). For comparison, SS316 was much more ductile at room temperature and showed a noticeable reduction in cross-sectional area and dimpled fracture surfaces indicative of microvoid coalescence and ductile failure (Fig. 3b). The brittle behavior of MA956 at room temperature was consistent with other reported results and is one of the primary disadvantages for its use in room temperature applications [23,25,27]. At elevated temperatures, MA956 exhibited noticeable reduction in cross-sectional area and very fine microvoid coalescence indicating a more ductile fracture than that observed at room temperature, a result consistent with the improved ductility observed during tensile testing (Fig. 4).

As shown in the stress strain curves of Fig. 2 and the fractography of Fig. 3, FG BM MA956 is brittle and exhibits moderate strain hardening at room temperature. True stress and true strain were calculated from the engineering stress and engineering strain curves in Fig. 2 up to the onset of necking for all temperatures tested (Fig. 5). Using the Holloman relationship (Eq. (2)) [49], values for the strain hardening coefficient (k) and strain hardening exponent (n) were calculated as a function of temperature (Fig. 6). The results demonstrate that, as temperature is increased, MA956 undergoes significantly less strain hardening, and at the maximum test temperature of 600 °C, FG MA956 exhibits almost perfectly plastic behavior.

$$\sigma_{\text{true}} = k\varepsilon_{\text{true}}^{n}. \tag{2}$$

3.2. Friction stir welded stir zone tensile behavior

At room temperature, all FSW specimens showed a significant reduction in strength and an increase in ductility compared to BM specimens (Fig. 7). It should be noted that the gage section was comprised of only SZ material, and thus, this result reflects the change in the tensile behavior of the SZ material, not the entire weld structure. The maximum reduction in strength was 42% compared to the BM and occurred for the highest heat input condition (500 RPM/25 MMPM). This value compared very closely to the observed 37% reduction in hardness for the same conditions reported previously [21]. The differences in strength at room temperature between the FSW conditions were small but support the overall conclusion presented previously that higher heat input conditions produce softer SZ microstructures based predominantly on the increased grain size as heat input is increased; however, these previous conclusions did not fully address changes from the BM to the stir zones of the friction stir welded conditions which will be analyzed in this research.

The results for the elevated temperature tests at 400 °C and 600 °C both showed that FSW reduces the strength of the BM at each temperature; however, the lowest heat input condition (400 RPM/100 MMPM) resulted in only a 19% reduction in strength at 600 °C compared to a 33% reduction in strength for the highest heat input

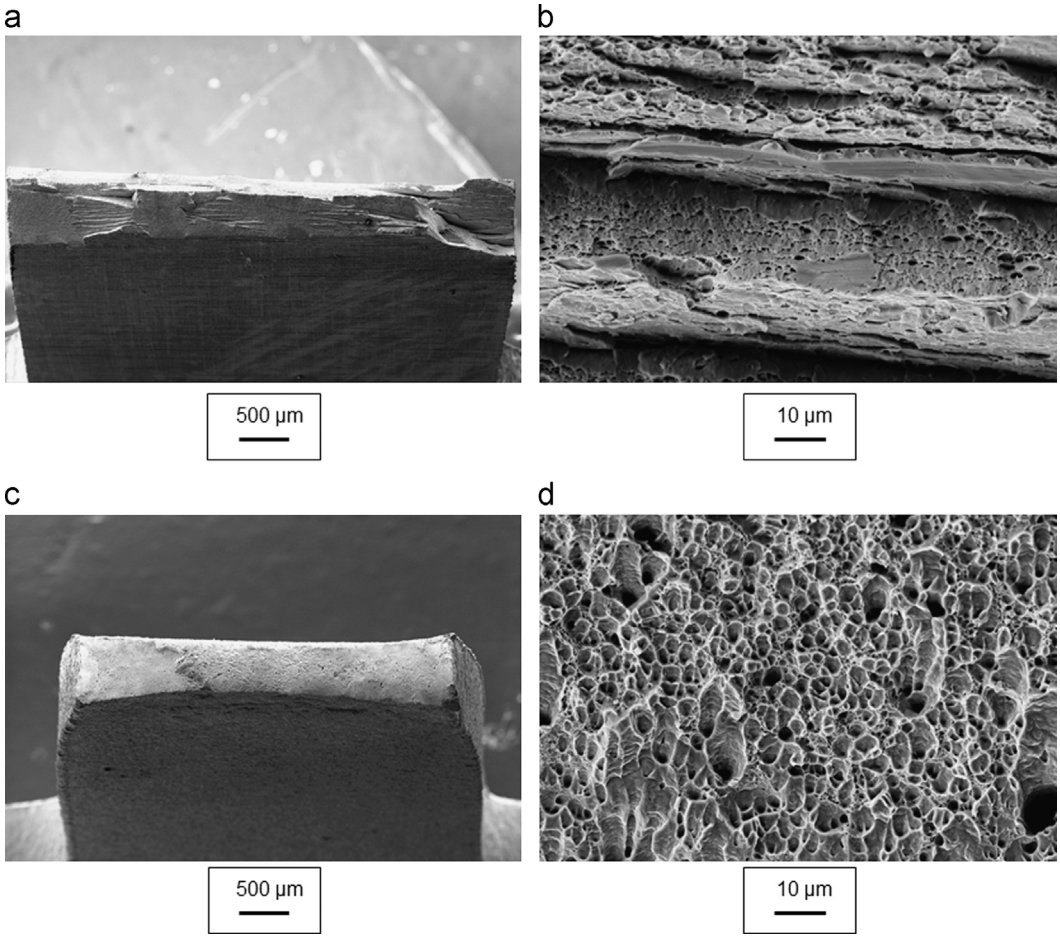

Fig. 3. Fractography of BM MA956 (a) at low magnification and (b) high magnification and SS316 (c) at low magnification and (d) high magnification all at room temperatures showing the brittle behavior of MA956 at room temperature.

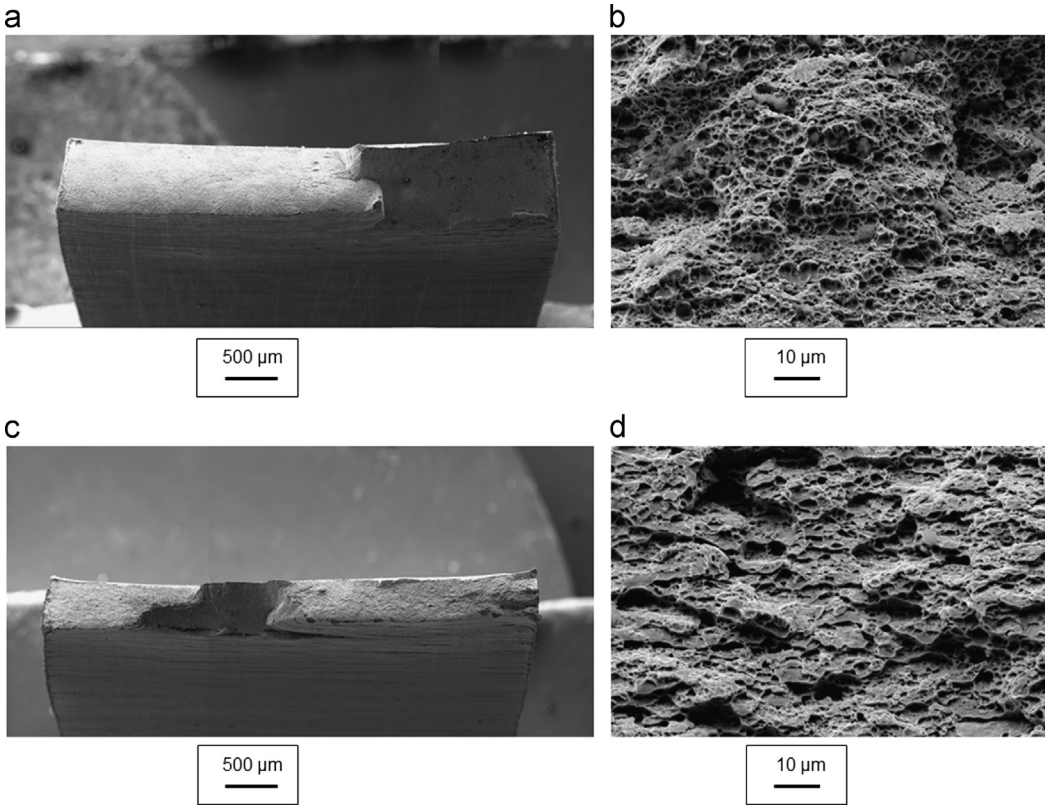

Fig. 4. Fractography of BM MA956 at 400 °C (a) at low magnification and (b) at high magnification and 600 °C (c) at low magnification and (d) at high magnification showing the increased ductility of MA956 at elevated temperatures compared to the brittle fracture at room temperature in Fig. 3.

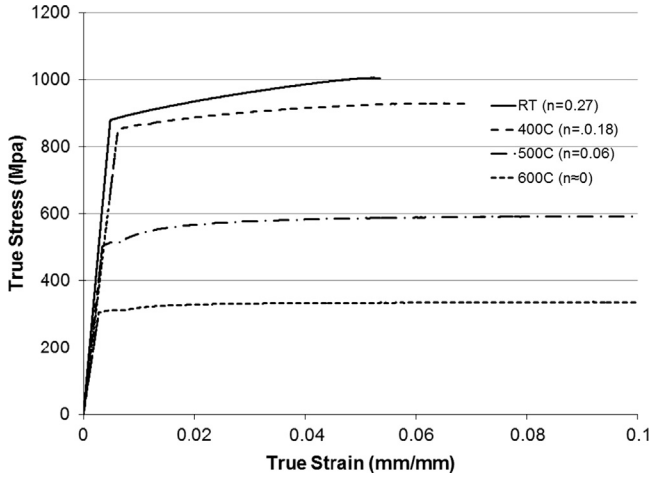

Fig. 5. True stress–strain curves for BM MA956 at various temperatures. True stress–strain values were calculated from the engineering stress–strain values (Fig. 2) to the onset of necking allowing for calculation of strain hardening exponent (n).

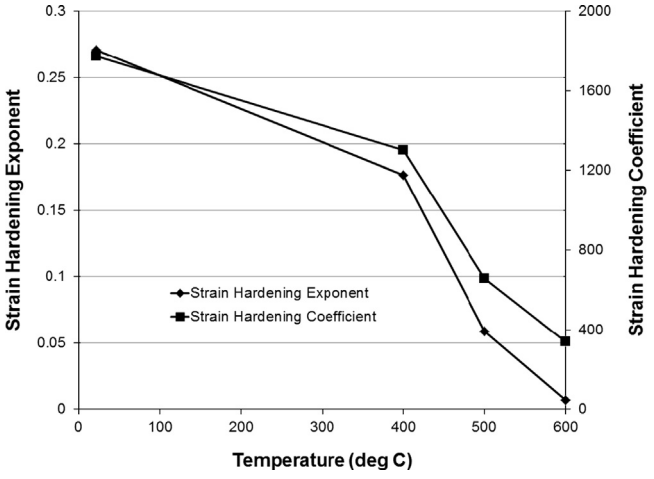

Fig. 6. Strain hardening exponent (n) and strain hardening coefficient (k) as a function of temperature for BM MA956 using the Holloman equation (Eq. (2)).

condition (500 RPM/25 MMPM) at the same temperature. This trend is consistent with previous research on FSW of MA956 which demonstrated that lower heat input conditions produce more favorable SZ conditions (less grain coarsening, less oxide particle coarsening, and a harder SZ profile). The trend in ductility following FSW is less consistent at elevated temperatures than at room temperatures. The consistency of yield and ultimate tensile strength measurements and relative inconsistency of percent elongation measurements for miniature tensile specimens is discussed in other literature [42]. For brevity the results of FSW samples at the maximum temperature of 600 °C are shown in Fig. 8 although the trends were similar for 400 °C.

Fractography of FSW specimens was consistent with observations during tensile testing at all temperatures including the change in ductility seen on the stress–strain curves from the BM condition. At room temperature, friction stir welded MA956 displayed a noticeable reduction in cross-sectional area, and fracture surfaces were no longer dominated by the faceted transgranular appearance seen in the BM, but rather showed very fine microvoid coalescence throughout most of the fracture surface indicating a predominance of ductile failure. This type of fracture surface occurred for all FSW conditions and is shown in Fig. 9 with corresponding images of the BM for reference contained in Fig. 3a. At elevated temperatures, all FSW specimens showed ductile behavior with the most marked change occurring

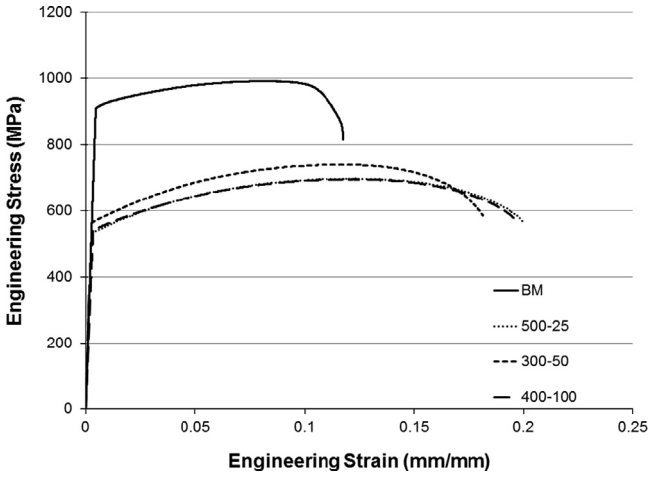

Fig. 7. Engineering stress–strain curves for BM MA956 and friction stir welded MA956 tested at room temperature showing a reduction in strength and increase in ductility following FSW.

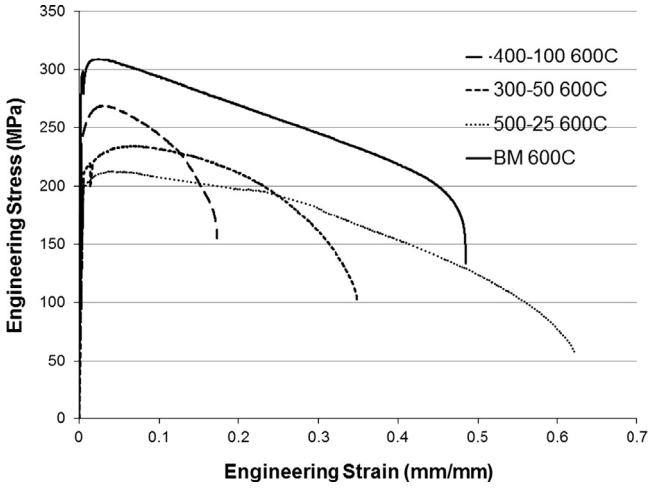

Fig. 8. Engineering stress–strain curves of friction stir welded MA956 tested at 600 °C.

for the highest heat input condition at the highest test temperature (Fig. 10) which also corresponds to the largest elongation measured in Fig. 2. As shown in Figs. 7 and 9, FSW caused an increase in ductility at room temperature; similarly the degree of strain hardening increased following FSW. The effect of FSW on ductility is less pronounced at elevated temperatures and thus the strain hardening behavior of FSW MA956 is similar to BM MA956 above room temperature.

4. Discussion

The grain size of MA956 is a dominant factor in controlling the tensile properties at room temperature. As mentioned previously, the MA956 used in this research is significantly finer in grain size (1–10 μm) than that normally supplied by Special Metals (> 100 μm). Comparative plots of strength (Fig. 11) and percent elongation (Fig. 12) show the differences between the FG alloy used in this research and the nominal CG alloy produced by Special Metals. The brittle behavior at room temperature of both FG and CG MA956 shown in Fig. 12 and the fractography of Fig. 3a is due to the low Ductile-Brittle Transition Temperature (DBTT) of MA956 which is stated as in the range of 0–100 °C by Special Metals [23] and corroborated by other sources [25,26,50].

FG MA956 is considerably stronger at lower temperatures than CG MA956, but this difference disappears as the temperature approaches 600 °C (Fig. 11). This difference in yield behavior can be entirely attributed to grain boundary strengthening described by the Hall–Petch relationship. Both FG and CG MA956 have limited ductility at room temperature (Fig. 12); however, FG MA956 shows improved ductility as the temperature increases. These trends combined with the improved radiation damage resistance of FG materials and comparable creep performance in some situations suggests that FG ODS alloys such as MA956 could be of benefit in nuclear material applications. Overcoming the obstacles in joining of these alloys would further promote their utility in these applications.

While FSW has already been demonstrated as a successful joining mechanism for MA956 and other ODS alloys, this research shows that FSW reduces the room temperature strength of MA956 significantly but improves the room temperature ductility of MA956 over a range of FSW heat inputs (Fig. 7). The overall strength comparison of BM to friction stir welded MA956 at elevated temperatures is shown in Fig. 13 and shows that at elevated temperature the effect of FSW on the yield strength of MA956 is much less noticeable. This initial observation suggests that the mechanisms behind the reduction in strength of friction stir welded MA956 are more complex than Hall–Petch grain boundary strengthening alone; however, these initial results are encouraging and support the use of both BM and friction stir welded FG MA956 at the elevated temperatures required for nuclear applications due to the relatively high retained strength of the weld.

The reduction in yield strength of the friction stir welded material compared to the base plate material can be explained primarily through a loss of dispersion strengthening and secondarily by a loss in grain refinement. The grain size of the SZ material has been previously shown to increase systematically with increasing FSW heat input [21]. Using SEM backscatter electron imaging (Fig. 14), we show that the yttrium aluminate oxide particles qualitatively increased in size in the SZ. In addition, the dislocation density was qualitatively much less in the SZ material following FSW (Fig. 15). A more comprehensive review of particle size and distribution following FSW using a variety of techniques and scales is presented elsewhere [22] although the conclusion that FSW causes significant oxide particle coarsening is paramount to the understanding of changes in tensile behavior following FSW. Table 3 contains a consolidated list of material and microstructural data on MA956 at room temperature as function of FSW conditions with values of HI included for reference. The BM value of average particle size was obtained from research by Hsiung on identical FG MA956 during research on nanoparticles in MA956 [51]. Table 3 shows several important room temperature results that occur following FSW: (1) yield strength, ultimate tensile strength, and hardness all decrease, (2) percent elongation increases, (3) ferrite grains are significantly coarsened, and (4) yttrium aluminum oxide particles are significantly coarsened. All of these effects with the exception of percent elongation are enhanced as the heat input during FSW is increased.

The change in yield strength of the SZ material following FSW can be explained in terms of its microstructural evolution. The yield strength of a material can be estimated as its intrinsic material yield strength summed with contributions by various strengthening mechanisms. This approach has been utilized by Badmos and Wang independently on both FG and CG MA956 to compare theoretical estimates to experimental processes [29–31]. In this paper, we will use the approach of approximating the overall strengthening response as a linear superposition of strengthening terms (Eq. (3)), although a root mean-square method has been proposed by Kocks [52] and used on MA956 [29] as well as other dispersion

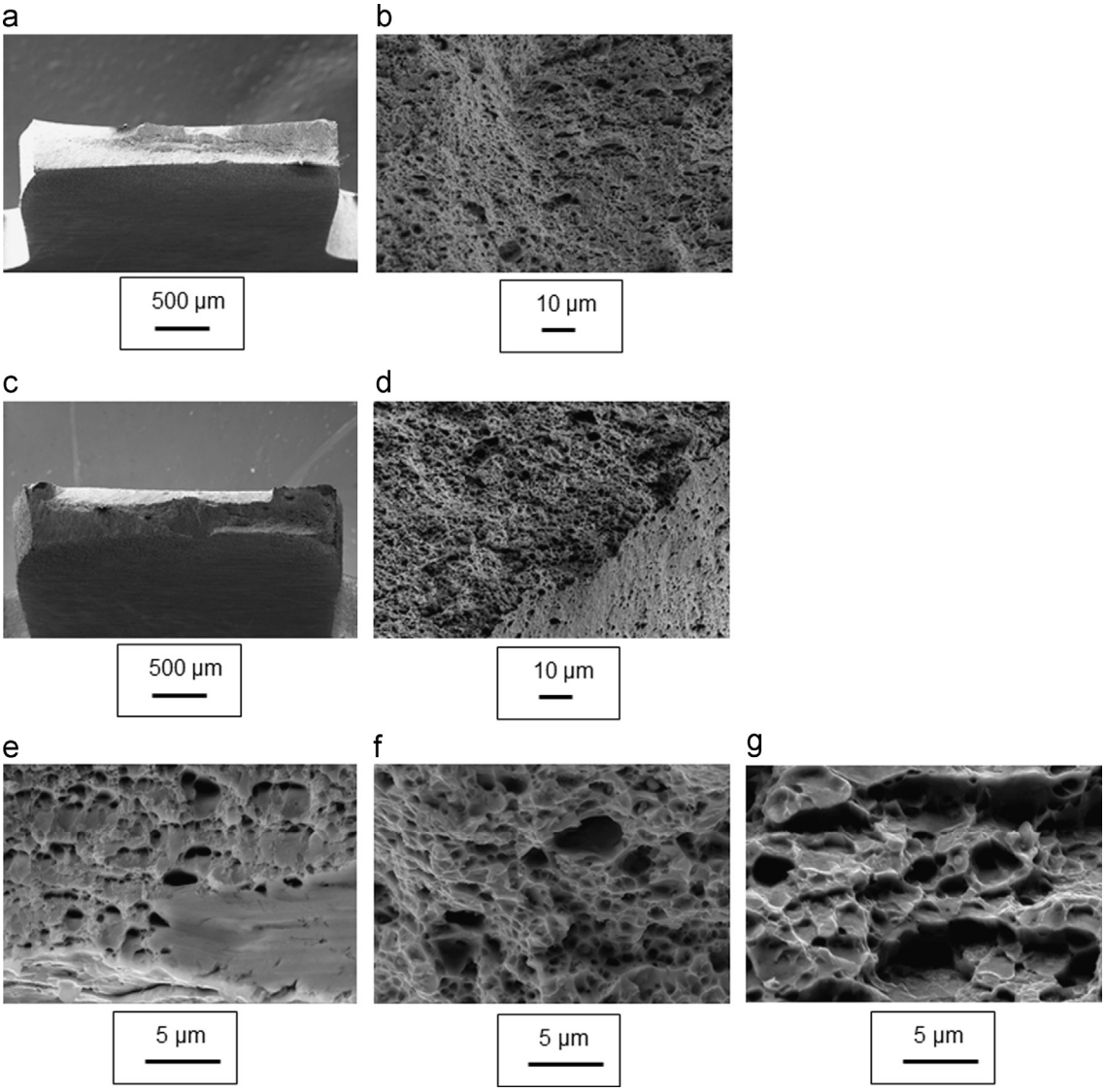

Fig. 9. Fractography of MA956 at room temperature for low heat input condition (400 RPM/100 MMPM) (a) at low magnification and (b) at high magnification, high heat input condition (500 RPM/25 MMPM) (c) at low magnification and (d) at high magnification, and high magnification images of (e) base metal, (f) low heat input condition, and (g) high heat input condition.

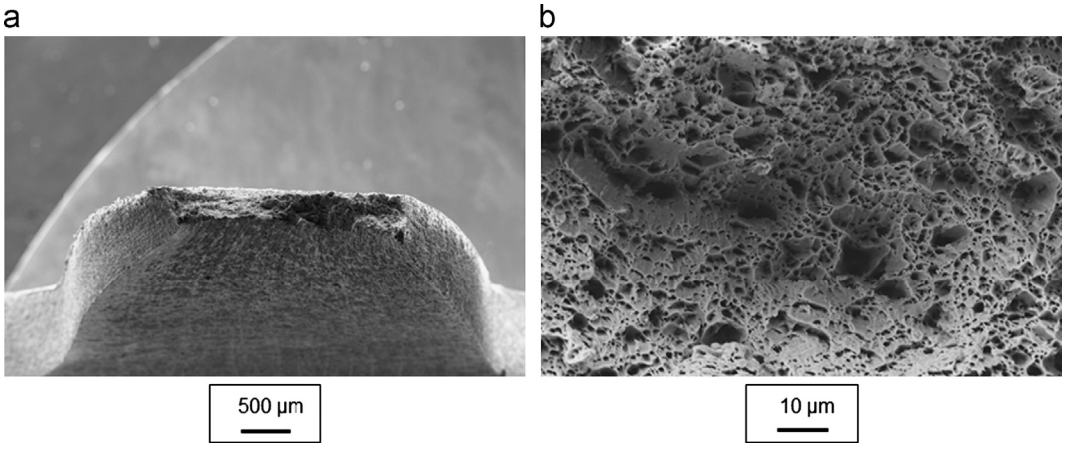

Fig. 10. Fractography of MA956 friction stir welded with high heat input conditions (500 RPM/25 MMPM) fractured in tension at 600 °C showing the largest amount of ductility corresponding to the highest test temperature and highest heat input condition (a) at low magnification and (b) at high magnification.

strengthened alloys such as 14YWT [53].

$$\sigma_y = \sigma_O + \sigma_{SS} + \sigma_{GB} + \sigma_P + \sigma_D \quad (3)$$

The strengthening contribution method proposed in Eq. (3) is defined as follows: the yield strength of a given material (σ_y) is equal to the sum of Peierls–Nabarro stress representing the

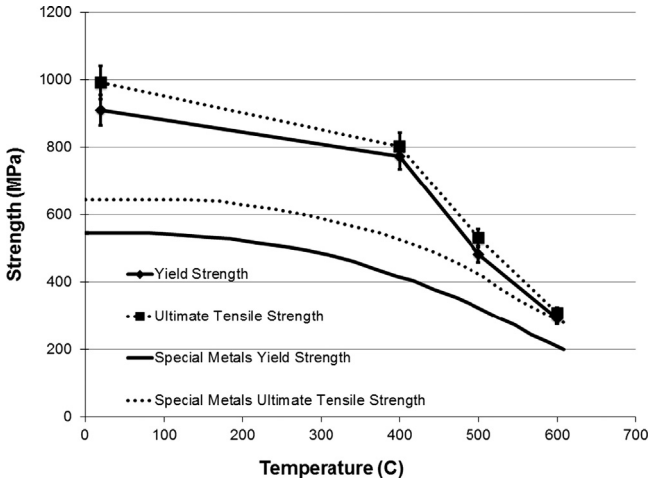

Fig. 11. Yield and ultimate strengths of fine grain unrecrystallized MA956 with comparison to manufacture's specifications for coarse grain recrystallized MA956 [23]. Error bars show 5% variation based on SS316 test results.

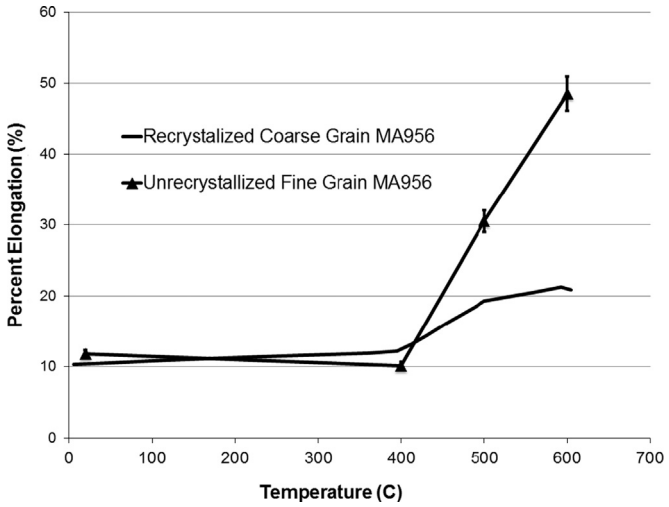

Fig. 12. Percent elongation of fine grain unrecrystallized MA956 with comparison Special Metals manufacture specifications of coarse grain recrystallized MA956 [23]. Error bars show 5% variation based on SS316 test results.

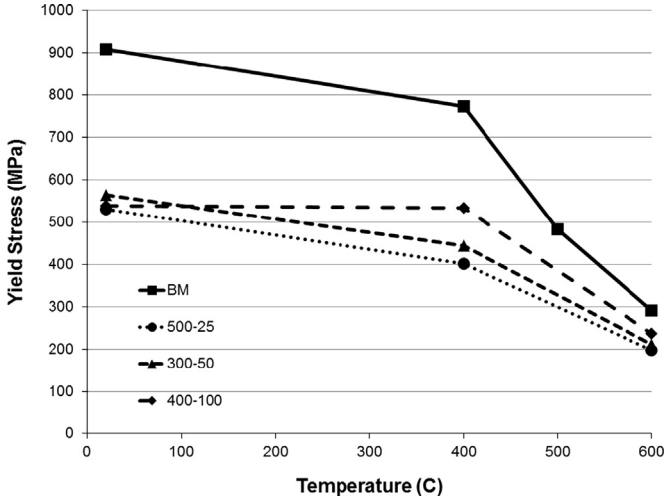

Fig. 13. Yield strength versus temperature for consolidated friction stir welded conditions. The softening effect of FSW is less evident at high temperature.

stress due to resistance of dislocation motion within the crystal lattice (σ_O), the strengthening contribution from solid solution strengthening (σ_{SS}), the strengthening contribution from grain boundary strengthening in accordance with the Hall–Petch relationship (σ_{GB}) (Eq. (4)), the strengthening contribution from oxide particle dispersion strengthening (σ_P), and the strengthening contribution from dislocation strengthening (σ_D). Because FSW is a solid state joining mechanism and MA956 maintains its body centered cubic (BCC) structure and average composition throughout the welding process, both σ_O and σ_{SS} are assumed to not change significantly during FSW. The remaining terms σ_{GB}, σ_P, and σ_D all change following FSW as suggested by data in Table 3 and the STEM images of Fig. 15.

$$\sigma_{GB} = kd^{-1/2} \tag{4}$$

The change in yield strength as the grain size changes is well-described by the Hall–Petch relationship. Using the data from Table 3, a Hall–Petch plot of MA956 was generated and the value of the Hall–Petch constant (k) in Eq. (4) was calculated to be 0.164 MPa $m^{1/2}$. Other research by Badmos and Wang both used estimated values of k (0.5 MPa $m^{1/2}$) based on MA956 being a ferritic stainless steel [29,30]. Fig. 16 shows that the yield strength for SZ material from all three FSW conditions fall on the Hall–Petch line. However, the yield strength of the BM condition does not fall on this line, but is instead 255 MPa higher in yield strength than its corresponding location on the Hall–Petch line for its grain size. This difference indicates that the reduction in strength from the BM to any of the FSW conditions is due primarily to changes in oxide particle dispersion strengthening and dislocation strengthening which combined should be approximately 255 MPa.

This estimate for strength loss is remarkably close to previous work examining strengthening mechanisms in MA956. Table 4 contains summary data from both Badmos and Wang for strengthening terms in Eq. (3) [29,30]. Both of these papers estimate the yield strength contribution due to oxide particle strengthening to be between 248–258 MPa, quite similar to the value of 255 MPa presented here. Research by Badmos was based on BM MA956, and the method used to calculate the 248 MPa contribution of particle strengthening was achieved by arc melting MA956 in argon causing the oxides to float off producing a resulting alloy that was no longer particle strengthened. The yield strength contribution due to oxide particle dispersion was estimated by Wang using an Orowan-type relation (Eq. (5) [29]), where the Taylor factor, M, was 2.7, the shear modulus, G, was 60 GPa, the Burgers vector, b, was 0.25 nm, and Poisson's ratio, ν, was 0.3. We can estimate the oxide particle dispersion strengthening component from the present data using Eq. (5) and values from Table 3 for average particle radius (r) and inter-particle spacing (λ). The present results show σ_P for SZ material is only 13.2 MPa for the low heat input condition (400 RPM/100 MMPM) and 13.9 MPa for the high heat input condition (500 RPM/25 MMPM). This estimate compares very favorably to the data in Fig. 16 which suggests that FSW causes the complete loss of particle strengthening even for the low heat input condition. This overall conclusion is also strongly supported by research by Kim on 14YWT which concluded that oxide particles greater than 100 nm in size (comparable to all oxide particles following FSW in this research) would result in σ_P being less than 50 MPa [53,54]. It is worth noting that particles in 14YWT are Y–Ti–O particles as opposed to the Y–Al–O particles in MA956 and the work by Kim did not include any conditions that would cause a comparable degree of particle coarsening as that seen here, but the calculation method used by Kim is very similar to that presented by Wang and used here in Eq. (5).

$$\sigma_{Oro} = M\frac{0.4}{\pi}\frac{Gb}{\sqrt{1-\nu}}\frac{\ln\left(\frac{2r}{b}\right)}{\lambda} \tag{5}$$

The tensile response data in this paper compares favorably with previous Vickers hardness measurements on the same material [21], suggesting that Vickers hardness is a reliable method for estimating

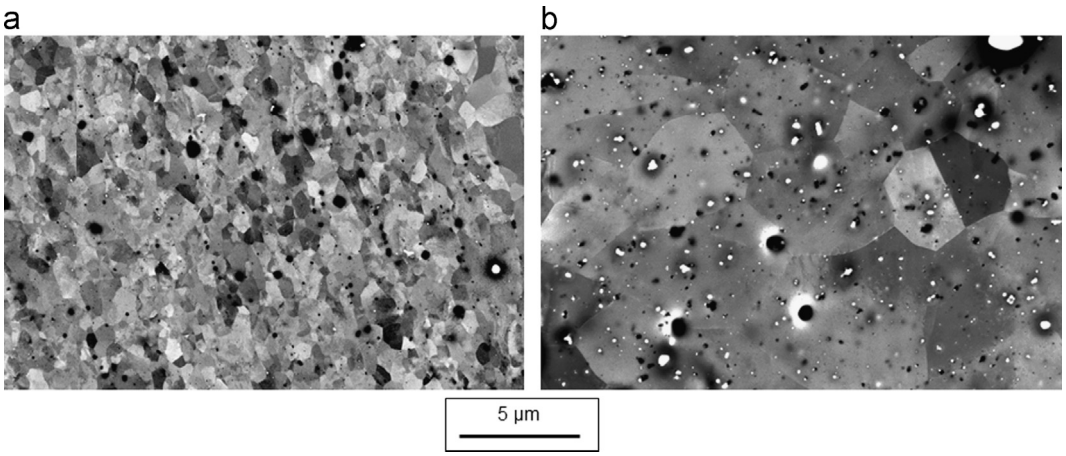

Fig. 14. SEM backscatter images of (a) BM MA956 and (b) friction stir welded MA956 with high heat input (500 RPM/25 MMPM) showing grain and oxide particle coarsening following FSW. Oxide particles appear as bright white particles in (b) and are not visible at this scale in (a).

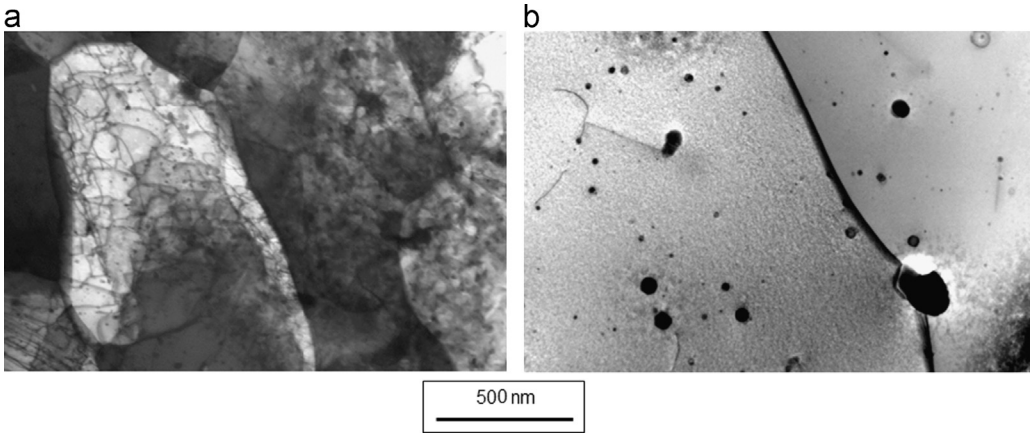

Fig. 15. Low voltage STEM images of (a) BM MA956 and (b) friction stir welded MA956 with low heat input (300 RPM/50 MMPM) showing a qualitative increase in grain size and reduction in dislocation density following FSW.

Table 3
Summary of processing, microstructure, and material property relationships of MA956 at room temperature following FSW with varying process parameters.

Weld condition	Heat index	σ_{YS} (MPa)	σ_{UTS} (MPa)	Hardness (H_V)	PE (%)	Ferrite grain size (μm)	Average oxide particle size (nm)	Average inter-particle spacing (μm)
BM	–	909	991	346	12	0.890	8.07 [51]	–
400-100	4	539	696	221	20	6.94	166	3.23
300-50	6	563	740	225	18	4.16	163	3.19
500-25	20	530	698	218	20	12.5	343	3.41

the tensile properties in friction stir welded steels. Although hardness is a measure of a material's plastic flow resistance and therefore a function of both yield strength and strain hardening, it can be used as an effective metric for changes in material performance following FSW. The maximum reduction in strength and hardness following FSW occurred for the highest heat input condition used (500 RPM/25 MMPM) which was consistent with hypotheses based on evolved microstructure. For the highest heat input condition (500 RPM/25 MMPM) room temperature yield strength was reduced by 42% with a corresponding 37% reduction in hardness reported previously. Using the Tabor relationship between hardness (H) and yield strength (Eq. (6)) which is common for materials with small values of n, approximate values of yield strength can be obtained from hardness results. Using experimental tensile properties values from this research, the yield strength predicted by the Tabor relationship can be compared to the actual tensile yield strength for the SZ material. These two quantities are within approximately 25% across the different FSW conditions.

$$\frac{H}{\sigma_y} \approx 3. \tag{6}$$

However, using experimentally determined values of n can result in improved accuracy when predicting yield strength from hardness data. In a comprehensive analysis of several metallic materials including aluminum, iron, stainless steel, and copper in a variety cold worked and annealed conditions, Jung developed best fit relationships between yield strength, ultimate tensile strength, Vickers hardness (H_V), and the strain hardening exponent, n (Eqs.

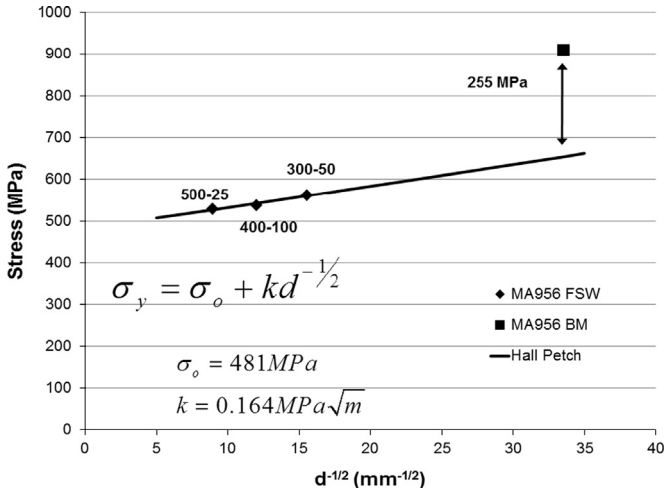

Fig. 16. Hall Petch plot of MA956 with varying grain size achieved by FSW. The difference in strength of the BM compared to the Hall Petch line is attributed to changes in particle and dislocation strengthening mechanisms.

Table 4
Theoretical strengthening contributions used by other authors for MA956 prior to FSW (σ_O—Peierls–Nabarro stress, σ_{SS}—strengthening contribution from solid solution strengthening, σ_P—strengthening contribution from particle strengthening, and σ_D—strengthening contribution from dislocation strengthening). Contribution from grain boundary strengthening (σ_{GB}) was calculated by each author using an assumed value of 0.5 MPa $m^{1/2}$ for the Hall–Petch constant, k and varied depending on the grain size.

Author	σ_O (MPa)	σ_{SS} (MPa)	σ_P (MPa)	σ_D (MPa)
Badmos [31]	36	116	248	31
Wang [29]	50	130	258	47

(7) and (8)) [42]. Using either of these relationships on the present data to calculate yield strength from hardness results in approximately 20% error across the FSW conditions used, a small improvement over the basic Tabor relationship. The relationship in Eqs. (7) and (8) are both strong functions of n. The values of n presented here were calculated from curve fits of Eq. (2) on the data given in Fig. 5. Improvements in the measurement and calculation of n could result in further improved consistency of relationships between hardness and yield strength.

$$\frac{\sigma_y}{H_V} = \frac{0.25^n}{3.4}. \quad (7)$$

$$\frac{\sigma_{uts}}{H_V} = \frac{2.5^n}{3.4}. \quad (8)$$

5. Conclusions

The tensile properties of FG MA956 as function of temperature and FSW conditions were investigated. The following conclusions were drawn:

(1) Similar to CG MA956, FG MA956 is brittle at room temperature, but FG MA956 has a higher yield and ultimate tensile strength than CG MA956 due to grain refinement. At room temperature FG MA956 undergoes moderate strain hardening (n=0.27). Above 400 °C FG MA956 shows improved ductility over CG MA956 up to the maximum temperature tested of 600 °C. At elevated temperatures FG MA956 exhibits very limited strain hardening and demonstrates nearly perfectly plastic behavior at 600 °C.

(2) FSW on FG MA956 results in up to a 42% reduction in yield strength of the SZ material for high heat input conditions. Reducing the heat input during FSW lessens this reduction in strength and at higher testing temperatures, the reduction in strength is less severe. FSW also causes an increase in ductility that is predominantly apparent at lower temperatures. When combined with microstructural data on the same FG MA956, the following effects are observed following FSW: yield and ultimate tensile strength at all temperatures are reduced, room temperature ductility is increased, hardness in the SZ is reduced (by approximately the same percent as strength), dislocation density in the SZ is reduced, grains in the SZ are significantly coarsened, and oxide particles in the SZ are significantly coarsened. All of these effects are enhanced as the heat input due to FSW is increased.

(3) Reduction in yield strength due to FSW is due to the combined effects mentioned above; however, the majority of the loss of strength when comparing the BM to the welded condition stems from the complete loss of oxide particle strengthening due to oxide particle coarsening following FSW. The differences in yield strength in SZ material amongst FSW conditions are well described by the Hall–Petch relationship.

(4) Material property evaluation by hardness measurements can be an accurate assessment method without having to conduct full tensile testing. Using established relationships of hardness to strength can produce reasonably accurate results while also showing correct trends following FSW.

(5) MA956 can be manufactured in a FG or CG form. FSW can produce consolidated welds in FG MA956 that can maintain up 80% of the base material's strength at 600 °C. Control of grain size during manufacture and the welding conditions during joining by FSW may produce a final welded material condition sufficient to meet high temperature material specifications.

Acknowledgments

This work in part was performed under the auspices of the U.S. Department of Energy by Lawrence Livermore National Laboratory under Contract DE-AC52-07NA27344.

We are grateful for assistance with microscopy sample preparation and data acquisition from Dr. E.S.K. Menon.

References

[1] S.J. Zinkle, N.M. Ghoniem, Fusion Engineering and Design 51–52 (2000) 55–72.
[2] S. Ukai, T. Nishida, H. Okada, T. Okuda, M. Fujiwara, K. Asabe, Journal of Nuclear Science and Technology 34 (1997).
[3] S. Ukai, T. Nishida, T. Okuda, T. Yoshitake, Journal of Nuclear Science and Technology 35 (1998) 294–300.
[4] I. Charit, K.L. Murty, C.C. Koch, Creep Properties of Advanced Steels For High Efficiency Power Plants, 2008.
[5] M.S. El-Genk, J.M. Tournier, Journal of Nuclear Materials 340 (2005) 93–112.
[6] B. van der Schaaf, D.S. Gelles, S. Jitsukawa, A. Kimura, R.L. Klueh, A. Moslang, et al., Journal of Nuclear Materials 283 (2000) 52–59.
[7] E.E. Bloom, S.J. Zinkle, F.W. Wiffen, Journal of Nuclear Materials 329 (2004) 12–19.
[8] R.J. Kurtz, A. Alamo, E. Lucon, Q. Huang, S. Jitsukawa, A. Kimura, et al., Journal of Nuclear Materials 386 (2009) 411–417.
[9] G.R. Odette, D.T. Hoelzer, Journal of the Minerals Metals and Materials Society 62 (2010) 84–92.
[10] S.J. Zinkle, G.S. Was, Acta Mater. 61 (2013) 735–758.
[11] M.G. McKimpson, D. Odonnell, JOM—Journal of the Minerals Metals and Materials Society 46 (1994) 49–51.
[12] R. Lindau, M. Klimenkov, U. Jaentsch, A. Moeslang, L. Commin, Journal of Nuclear Materials 416 (2011) 22–29.
[13] H.J.K. Lemmen, K.J. Sudmeijer, I.M. Richardson, S. van der Zwaag, Journal of Materials Science 42 (2007) 5286–5295.

[14] V.G. Krishnardula, N.I. Sofyan, W.F. Gale, J.W. Fergus, Transactions of the Indian Institute of Metals 59 (2006) 199–203.
[15] S. Noh, R. Kasada, A. Kimura, S.H.C. Park, S. Hirano, Journal of Nuclear Materials 417 (2011) 245–248.
[16] F. Legendre, S. Poissonnet, P. Bonnaillie, L. Boulanger, L. Forest, Journal of Nuclear Materials 386-388 (2009) 537–539.
[17] A. Etienne, N.J. Cunningham, Y. Wu, G.R. Odette, Materials Science and Technology 27 (2011) 724–728.
[18] W. Han, S. Ukai, F. Wan, Y. Sato, B. Leng, H. Numata, et al., Materials Transactions 53 (2012) 390–394.
[19] W.T. Han, F.R. Wan, B. Leng, S. Ukai, Q.X. Tang, S. Hayashi, et al., Science and Technology of Welding and Joining 16 (2011) 690–696.
[20] B.K. Jasthi, S.M. Howard, W.J. Arbegast, G.J. Grant, S. Koduri, D.R. Herling, in: Friction Stir Welding Processing III, San Francisco, CA, 2005, pp. 75–79.
[21] B.W. Baker, L.N. Brewer, E.S.K. Menon, T.R. McNelley, B. El-dasher, S. Torres, et al., in: R.S. Mishra, M.W. Mahoney, S. Yutaka, Y. Hovanski, R. Verma (Eds.), Friction Stir Welding and Processing VII, Wiley, Warrendale, PA 2013.
[22] B.W. Baker, Processing, microstructure, and material property relationships following friction stir welding of oygen dispersion strengthened steels, (Ph.D. dissertation), Mechanical and Aerospace Engineering Department, Naval Postgraduate School, Monterey, CA, 2013.
[23] SpecialMetalsCorporation, Engineering Data Sheet for Incoloy MA956 SMC-008, 2004.
[24] SpecialMetals and B.W. Baker, Personal Communication, 2013.
[25] B. Dubiel, W. Osuch, M. Wrobel, P.J. Ennis, A. Czyrskafilemonowicz, Journal of Materials Processing Technology 53 (1995) 121–130.
[26] M. Bartsch, A. Wasilkowska, A. Czyrska-Filemonowicz, U. Messerschmidt, Materials Science and Engineering A-Structural Materials Properties Microstructure and Processing 272 (1999) 152–162.
[27] J. Chao, J.L. Gonzalez-Carrasco, J. Ibanez, M.L. Escudero, G. Gonzalez-Doncel, Metallurgical and Materials Transactions A-Physical Metallurgy and Materials Science 27 (1996) 3809–3816.
[28] J.D. Whittenberger, Metallurgical Transactions A-Physical Metallurgy and Materials Science 12 (1981) 845–851.
[29] J. Wang, W. Yuan, R.S. Mishra, I. Charit, Journal of Nuclear Materials 432 (2013) 274–280.
[30] A.Y. Badmos, H. Bhadeshia, Materials Science and Technology 14 (1998) 1221–1226.
[31] A.Y. Badmos, H. Bhadeshia, D.J.C. MacKay, Materials Science and Technology 14 (1998) 793–809.
[32] R.J. Salomon, Journal De Physique IV 3 (1993).
[33] B. Wilshire, Creep processes in dispersion-strengthened alloys, in: E.M. Taleff, C.K. Syn, D.R. Lesuer (Eds.), Deformation, Processing, and Properties of Structural Materials: Symposium Honoring Professor Oleg D Sherby, 2000.
[34] B. Wilshire, Creep mechanisms in oxide-dispersion-strengthened alloys, in: J.C Earthman, F. A. Mohamed (Eds.), Creep and Fracture of Engineering Materials and Structures, Minerals, Metals, and Materials Society, 1996 19–28, Publisher is Minerals, Metals, and Materials Society Warrendale, PA.
[35] R.L. Klueh, P.J. Maziasz, I.S. Kim, L. Heatherly, D.T. Hoelzer, N. Hashimoto, et al., Journal of Nuclear Materials 307 (2002) 773–777.
[36] R.L. Klueh, J.P. Shingledecker, R.W. Swindeman, D.T. Hoelzer, Journal of Nuclear Materials 341 (2005) 103–114.
[37] M. West, B. Jahsthi, P. Hosemann, V. Sodesetti, Friction Stir Welding and Processing VI, TMS, Warrendale, PA (2011) 2011; 33–40.
[38] R.S. Mishra, Z.Y. Ma, Materials Science and Engineering R-Reports 50 (2005) 1–78.
[39] S.K. Chimbli, D.J. Medlin, W.J. Arbegast, Minimizing Lack of Consolidation Defects in Friction Stir Welds, 2007.
[40] P. Biswas, D.A. Kumar, N.R. Mandal, Proceedings of the Institution of Mechanical Engineers Part B-Journal of Engineering Manufacture 226 (2012) 641–648.
[41] R. Nandan, T. DebRoy, H.K.D.H. Bhadeshia, Progress in Materials Science 53 (2008) 980–1023.
[42] P. Jung, A. Hishinuma, G.E. Lucas, H. Ullmaier, Journal of Nuclear Materials 232 (1996) 186–205.
[43] K. Noda, K. Ehrlich, S. Jitsukawa, A. Moslang, S. Zinkle, Journal of Nuclear Materials 258 (1998) 97–105.
[44] A. Kohyama, K. Hamada, H. Matsui, Journal of Nuclear Materials 179 (1991) 417–420.
[45] W.J. Yuan, Z.L. Zhang, Y.J. Su, L.J. Qiao, W.Y. Chu, Materials Science and Engineering A-Structural Materials Properties Microstructure and Processing 532 (2012) 601–605.
[46] J.D. Lord, B. Roebuck, R. Morrell, T. Lube, Materials Science and Technology 26 (2010) 127–148.
[47] Y.H. Zhao, Y.Z. Guo, Q. Wei, T.D. Topping, A.M. Dangelewicz, Y.T. Zhu, et al., Materials Science and Engineering A-Structural Materials Properties Microstructure and Processing 525 (2009) 68–77.
[48] P. Han, Tensile Testing, ASM International, Materials Park, Ohio, 1992.
[49] M. Meyers, K. Chawla, Mechanical Behavior of Materials, 2nd ed., Cambridge University Presss, Cambridge, NY, 2009.
[50] A. Alamo, H. Regle, J.L. Bechade, in: J.M. Capus, R.M. German (Eds.), Advances in Powder Metallurgy & Particulate Materials – 1992, vol. 7: Novel Powder Processing, 1992, pp. 169–182.
[51] L.L. Hsiung, M.J. Fluss, S.J. Tumey, B.W. Choi, Y. Serruys, F. Willaime, et al., Physical Review B 82 (2010).
[52] U.F. Kocks, A.S. Argon, M.F. Ashby, Progress in Materials Science 19 (1975) 1–281.
[53] J.H. Kim, T.S. Byun, D.T. Hoelzer, C.H. Park, J.T. Yeom, J.K. Hong, Materials Science and Engineering A-Structural Materials Properties Microstructure and Processing 559 (2013) 111–118.
[54] J.H. Kim, T.S. Byun, D.T. Hoelzer, S.W. Kim, B.H. Lee, Materials Science and Engineering A-Structural Materials Properties Microstructure and Processing 559 (2013) 101–110.